

This document is confidential and is proprietary to the American Chemical Society and its authors. Do not copy or disclose without written permission. If you have received this item in error, notify the sender and delete all copies.

Mid-infrared plasmon-enhanced spectroscopy with germanium antennas on silicon substrates

Journal:	<i>Nano Letters</i>
Manuscript ID	nl-2015-03247s.R1
Manuscript Type:	Communication
Date Submitted by the Author:	08-Oct-2015
Complete List of Authors:	Baldassarre, Leonetta; Università di Roma La Sapienza; Istituto Italiano di Tecnologia Sakat, Emilie; Politecnico di Milano, Frigerio, Jacopo; Politecnico di Milano, Samarelli, Antonio; University of Glasgow, Gallacher, Kevin; University of Glasgow, Calandrini, Eugenio; Università di Roma La Sapienza, Isella, Giovanni; Politecnico di Milano, Paul, Douglas; University of Glasgow, Ortolani, Michele; Sapienza University of Rome, Physics Dept. Biagioni, Paolo; Politecnico di Milano, Physics

SCHOLARONE™
Manuscripts

Mid-infrared plasmon-enhanced spectroscopy with germanium antennas on silicon substrates

Leonetta Baldassarre^{1,2,‡}, Emilie Sakat^{3,‡}, Jacopo Frigerio⁴, Antonio Samarelli⁵, Kevin Gallacher⁵, Eugenio Calandrini¹, Giovanni Isella⁴, Douglas J. Paul⁵, Michele Ortolani¹, Paolo Biagioni^{3,}*

¹Dipartimento di Fisica, Università di Roma “La Sapienza”, Piazzale Aldo Moro 5, I-00185
Roma, IT

²Center for Life Nano Science@Sapienza, Istituto Italiano di Tecnologia, Viale Regina Elena
291, I-00161 Roma, IT

³Dipartimento di Fisica, Politecnico di Milano, Piazza Leonardo da Vinci 32, I-20133 Milano, IT

⁴LNESS, Dipartimento di Fisica del Politecnico di Milano, polo di Como, via Anzani 42,
I-22100 Como, IT

⁵School of Engineering, University of Glasgow, Rankine Building, Oakfield Avenue, Glasgow
G12 8LT, UK

1
2
3 ABSTRACT
4
5
6

7 Mid-infrared plasmonic sensing allows the direct targeting of unique vibrational fingerprints of
8 molecules. While gold has been used almost exclusively so far, recent research has focused on
9 semiconductors with the potential to revolutionize plasmonic devices. We fabricate antennas out
10 of heavily-doped Ge films epitaxially grown on Si wafers and demonstrate up to two orders of
11 magnitude signal enhancement for the molecules located in the antenna hot spots compared to
12 those located on a bare silicon substrate. Our results set a new path towards integration of
13 plasmonic sensors with the ubiquitous CMOS platform.
14
15
16
17
18
19
20
21
22
23
24
25
26

27 KEYWORDS Silicon Technology, Plasmonics, Mid-Infrared Spectroscopy, Explosives
28
29
30 Detection
31
32
33
34
35
36
37
38
39
40
41
42
43
44
45
46
47
48
49
50
51
52
53
54
55
56
57
58
59
60

1
2
3 TEXT
4
5
6

7 Localized plasmon resonances are nowadays recognized as one of the most powerful
8 mechanisms to boost the interaction between light and matter at the nanoscale. In this frame,
9 recent plasmonic research has searched for novel material platforms which can improve the
10 quality and integrability of plasmonic interfaces and devices [1]. The choice of the material can
11 impact on the crystalline and nanofabrication quality of the device, the spectral range of
12 operation, and the amount of loss. The crucial issue for the future use of plasmonics in everyday
13 applications, however, is the integration with the Si-complementary metal-oxide semiconductor
14 (CMOS) technology process. This is difficult to foresee using the most common metal in
15 plasmonics, gold, due to it being a deep level impurity and a fast diffuser which is incompatible
16 with silicon technology. Among all applications of plasmonics, molecular sensing has already
17 made its way to the market. Plasmonic sensors can be based on refractive index variations at the
18 metal surface [2, 3], on the local enhancement of the electric field for Raman spectroscopy [4, 5],
19 or on the modification of the engineered transmitted or reflected wavefront in antennas by a
20 resonant molecular vibration in the mid-infrared (IR) [4, 6-16]. In the last few years the latter
21 approach, mainly pursued with the nanofabrication of gold antennas, led to reported signal
22 enhancements exceeding three orders of magnitude for the material located in the antenna hot
23 spots compared to the material outside the hotspots.
24
25
26
27
28
29
30
31
32
33
34
35
36
37
38
39
40
41
42
43
44
45
46

47 While metals are the most natural choice for visible and near-IR plasmonics, it has been
48 suggested that heavily-doped semiconductors (i.e. degenerately-doped to be metallic) could
49 replace and, possibly, outperform metals in the mid-IR frequency range [1, 14-25]. The
50 envisioned advantages for plasmonic device design include (i) the low absolute values of the
51 dielectric constant in the mid-IR, strictly resembling that of metals in the visible and near-IR
52
53
54
55
56
57
58
59
60

1
2
3 range but without the detrimental effect of interband transition losses, (ii) the high material
4 quality, thanks to single-crystalline epitaxial growth, (iii) in the case of foundry-compatible
5 group-IV semiconductors like Si and Ge, the potential for on-chip integration of antennas,
6 detectors and readout electronics, all fabricated in a single cost-effective silicon foundry
7 manufacturing process, and (iv) the possibility of active electrical and/or optical tuning of the
8 plasmonic effects by the control of the doping level. The onset of the plasmonic behavior of a
9 conducting material is marked by the so-called plasma frequency ω_p , i.e. the frequency below
10 which the real part of the dielectric constant of the material becomes negative. Standard doping
11 of semiconductors usually sets ω_p in the far-IR, while entering the mid-IR range requires high
12 doping levels, n up to 10^{19} - 10^{20} cm^{-3} according to the scaling law $\omega_p \propto \sqrt{\frac{n}{m_e}}$, m_e being the
13 electron effective mass.
14
15
16
17
18
19
20
21
22
23
24
25
26
27
28
29
30
31

32 In particular, the development of a plasmonic platform for molecular sensing based on group-
33 IV semiconductors [20-25] could have a dramatic impact on chemical or biological laboratory
34 applications because it could lead to the automation of surface-enhanced IR absorption
35 spectroscopy (SEIRA) [26] by exploiting readily and massively available disposable substrates
36 with integrated readout produced by standard silicon foundry processes. In the long term,
37 semiconductor plasmonic integration could lead to low-cost, compact and efficient lab-on-a-chip
38 devices for in-situ medical diagnostics, environmental monitoring in addition to safety and
39 security sensing. Also, whilst the performance of semiconductor plasmonic antennas may not be
40 the highest among all possible materials due to unavoidable losses in heavily doped materials,
41 the ability to integrate readout electronics and reference standards close to the detectors may be
42
43
44
45
46
47
48
49
50
51
52
53
54
55
56
57
58
59
60

1
2
3 key to optimize the sensitivity, specificity and speed of the full sensor system, as has already
4
5 been demonstrated e.g. in the development of CMOS single photon detector arrays [27].
6
7

8
9 In the last decade epitaxial Ge on Si has become a key technology for silicon photonics due to
10
11 its demonstrated compatibility with the CMOS technology [28-30]. Band engineering and doping
12
13 have already allowed for the demonstration of high-performance Ge photodiodes [31], optical
14
15 modulators [32, 33], prototype near-IR and far-IR LEDs and laser diodes [34-36], and integrated
16
17 systems [37]. Intrinsic Ge is also considered one of the best candidates for dielectric waveguides
18
19 in the mid-IR range of interest for molecular sensing (wavelengths $\lambda \sim 20$ to $4 \mu\text{m}$, or frequency
20
21 $\omega \sim 500$ to 2500 cm^{-1}) [38, 39]. The preference of Ge over Si is due to negligible absorption losses
22
23 compared to Si [30], which instead features relatively strong IR-active transitions in the 400-
24
25 1700 cm^{-1} range related to the presence of in-gap defect states. Such Si dipole-active impurity
26
27 states result in a large number of narrow absorption lines that may overlap to the weak molecular
28
29 signals of surface-enhanced sensors and complicate their interpretation [40]. Ge, on the other
30
31 side, displays no impurity absorption lines in the $100\text{-}2000 \text{ cm}^{-1}$ range and therefore it is
32
33 commonly employed for thick mid-IR optical elements such as lenses and prisms. For
34
35 applications in mid-IR plasmonics, in particular, Ge has been rarely if at all been used despite the
36
37 appealing perspective of combining infrared spectroscopy with CMOS integration. When
38
39 compared with Si, it has the advantage of a smaller electron effective mass ($m_e \approx 0.12$ for n-type
40
41 Ge and $m_e \approx 0.26$ for n-type Si), which widens the range of applications of plasmonic sensing
42
43 (allowing for higher ω_p) for a given doping level. This is especially relevant because of the
44
45 technological issues in achieving extremely high doping levels and because plasmonic losses in
46
47 doped semiconductors are also influenced by free-carrier scattering by charged impurities,
48
49 thereby favoring materials that can achieve higher plasma frequencies for a given doping level.
50
51
52
53
54
55
56
57
58
59
60

1
2
3 In this work we grow epitaxial Ge films on standard Si wafers using the low-energy plasma-
4 enhanced chemical vapor deposition (LEPECVD, see Supporting Information, Section A)
5 method [41, 42] and exploit phosphorus as the donor to achieve a doping level $n \approx 2.3 \cdot 10^{19} \text{ cm}^{-3}$,
6 thus setting $\omega_p \approx 1000 \text{ cm}^{-1}$ ($\approx 10 \text{ }\mu\text{m}$ wavelength). Micrometer-sized antennas are fabricated out
7 of the epitaxial Ge material by electron-beam lithography and reactive ion etching processes and
8 are characterized by Fourier-transform IR (FTIR) spectroscopy demonstrating localized plasmon
9 resonances in the $400 - 900 \text{ cm}^{-1}$ range. Finally, the fabricated devices are used for plasmon-
10 enhanced sensing experiments, detecting the vibrational fingerprints of thin molecular films and
11 liquids and demonstrating signal enhancements of up to two orders of magnitude when the target
12 materials are located at the antenna hotspots.
13
14
15
16
17
18
19
20
21
22
23
24
25
26
27

28 In order to design the antenna samples, we employ frequency- and time-domain simulations
29 (see Supporting Information, Section A). The dielectric constant of the Ge material for
30 simulations is obtained by numerical fitting of the reflection and transmission FTIR data
31 obtained from unpatterned Ge films in the entire infrared range (see Supporting Information,
32 Section B). The investigated antenna designs, demonstrated in Fig. 1, have fixed thickness and
33 width of the order of $1 \text{ }\mu\text{m}$ (i.e. comparable with the skin depth of the doped Ge in the $400 -$
34 900 cm^{-1} range) and a range of arm lengths L varying from 1 to $4 \text{ }\mu\text{m}$ (see Supporting
35 Information, Section C). We considered both single-arm (gapless) and double-arm (gap)
36 antennas. The simulations reveal the existence of two longitudinal antenna resonances related to
37 two distinct plasmonic modes propagating along the antenna arms. The first mode ('substrate-
38 like', labelled as R1) lies in the $300-500 \text{ cm}^{-1}$ range with the hotspots located at the Si/Ge
39 interface, while the second mode ('air-like', R2) lies in the $800 - 900 \text{ cm}^{-1}$ range with hotspots at
40 the upper antenna edges towards the air half-space. Field intensity maps of the two modes at
41
42
43
44
45
46
47
48
49
50
51
52
53
54
55
56
57
58
59
60

1
2
3 their respective near-field resonance frequencies are presented in Fig. 1. It should be stressed
4 here that a slight spectral shift occurs between the near-field and far-field resonances of the
5 investigated antennas (see Supporting Information, Section C), which is common for lossy
6 plasmonic materials [43]. The electromagnetic origin of the two modes is the same in single-arm
7 and double-arm antennas. The presence of the gap, however, affects the local intensity
8 distribution, further boosting the enhancement and confinement of the field. The evidence for
9 these two modes has already been reported in the literature [17-19]. In particular, the air-like R2
10 mode is the most promising mode for sensing applications because (i) the fields are located
11 towards the air half-space and therefore interact more effectively with the molecules to be
12 detected and (ii) the higher frequency compared to R1 is an advantage in view of the inherent
13 difficulty in growing high-quality semiconductor materials with heavy doping and therefore with
14 high plasma frequency.
15
16
17
18
19
20
21
22
23
24
25
26
27
28
29
30
31

32
33 A representative scanning electron microscopy (SEM) image of a fabricated gap antenna
34 sample is presented in Fig. 2a. The gap between the two arms is 300 nm, while the period for the
35 array is large enough to avoid significant near-field interactions between neighboring antennas.
36 The samples are characterized by FTIR spectroscopy, measuring both the transmission and
37 reflection spectra at normal incidence with the electric field linearly polarized along the antenna
38 axis as sketched in Fig. 2b. In the perspective of an integrated CMOS sensing device, however, it
39 is worth discussing the antenna signatures in reflection geometry. Indeed the use of an optical
40 scheme based on reflection instead of transmission is key in developing realistic mid-IR
41 chemical sensing devices as it can be coupled to e.g. a sensing chip equipped with microfluidics
42 (aqueous solutions are not transparent at mid-IR frequencies) [6]. Additionally, the measured
43
44
45
46
47
48
49
50
51
52
53
54
55
56
57
58
59
60

1
2
3 transmission suffers from light diffusion coming from the backside roughness [17] and from
4
5 absorptions in a thick Si substrate with a standard concentration of impurities [30].
6
7

8
9 Fig. 2b-d demonstrates a comparison between the calculated and measured reflection and
10 extinction spectra of three different antennas, namely two single-arm antennas with lengths
11 $L = 2.0 \mu\text{m}$ and $3.0 \mu\text{m}$, respectively, and one gap antenna with $L = 2.0 \mu\text{m}$ for the individual
12 antenna arms. In order to extract the antenna response, we demonstrate in Fig. 2b-d a normalized
13 extinction $E_{\text{norm}} = 1 - \frac{T_{\text{ant}}}{T_{\text{Si}}}$, with T_{ant} and T_{Si} being the transmission spectra acquired from the
14 antenna sample and from the bare Si substrate, respectively, and the reflection $R = \frac{R_{\text{ant}}}{R_{\text{Au}}}$, with R_{ant}
15 and R_{Au} being the reflection spectra acquired from the antenna sample and from a bare Au
16 mirror, respectively. The experimental results (solid lines in the left column) clearly display two
17 resonances corresponding to the R1 and R2 modes described before. Noticeably, the two spectral
18 features are not present in geometrically identical antennas fabricated out of lightly doped Ge on
19 Si ($n \approx 1.5 \cdot 10^{17} \text{ cm}^{-3}$ and $\omega_p < 100 \text{ cm}^{-1}$, dashed lines), which acts as a purely dielectric material
20 in the investigated frequency range, thus demonstrating that the resonances observed in the
21 doped samples are due to localized plasmons of the conduction electrons. This is also in
22 agreement with the redshift of the resonances with increasing arm length (compare the spectra of
23 2- and 3- μm single-arm antennas in Figs. 2b and 2d), as expected for plasmonic antennas [44].
24
25 We have also verified that the two strong resonant features disappear when the excitation electric
26 field is oriented perpendicular to the antenna axis and only the much weaker transverse
27 resonances are excited (see Supporting Information, Section E).
28
29
30
31
32
33
34
35
36
37
38
39
40
41
42
43
44
45
46
47
48
49
50
51
52
53
54

55 The simulated spectra at normal incidence for the investigated antenna samples, also displayed
56 in Fig. 2b-d, are in excellent agreement with the experiments, with small discrepancies that can
57
58
59
60

1
2
3 be attributed mainly to uncertainties in the value of the dielectric constant. Calculations have also
4
5 been performed to confirm that no collective behavior contributes to the R1 and R2 resonance
6
7 mechanisms. The spectral positions of the resonances have been found to be largely independent
8
9 of the incidence angle of excitation and periodicity of the array (see Supporting Information,
10
11 Section C and E), which highlights the localized character of the two resonances and confirms
12
13 that we are indeed addressing the plasmonic response of individual antennas. This paves the way
14
15 towards engineered devices where individual semiconductor antennas, each one with a specific
16
17 spectral response, are integrated on the same miniaturized silicon chip. Only in the case of Fig.
18
19 2d, the reader should notice that the asymmetric shape of the peak around 400 cm^{-1} is due to the
20
21 occurrence of a Rayleigh anomaly, as thoroughly discussed in the Supporting Information
22
23 (Section C).
24
25
26
27
28
29

30 With this understanding of the plasmonic properties of the antenna samples, we have explored
31
32 the potential for sensing using a reflection geometry, which is best suited for on-chip integrated
33
34 antennas. We have exploited the R2 resonance for the sensing of both thin solid-state layers and
35
36 liquid-phase droplets of substances with vibrational fingerprints in the spectral window covered
37
38 by R2.
39
40
41
42

43 In a first experiment (see Fig. 3), we have coated the same antennas of Fig. 2 with a
44
45 polydimethylsiloxane (PDMS) layer, which features a vibrational absorption resonance at
46
47 800 cm^{-1} (see Supporting Information, Section F) due to the Si-C bond stretching modes. This
48
49 absorption line matches very well the spectral position of the R2 near-field resonance of the
50
51 antennas, as demonstrated in Fig. S4 of the Supporting Information. By spin-coating the highly
52
53 diluted PDMS and further curing, we obtained a PDMS thickness below 40 nm, as demonstrated
54
55 in the SEM cross-section images of the PDMS-coated Ge antennas (obtained by the slice-and-
56
57
58
59
60

1
2
3 view technique with a dual electron and ion beam apparatus) in Fig. 3a. Reflection spectra for the
4 antenna samples are displayed in Fig. 3b. A comparison between the reflection spectra of the
5 clean samples (dashed lines) and of the spin-coated samples (solid lines), reveal that the PDMS
6 layer induces two changes in the spectra: a slight redshift of the plasmonic resonance, due to the
7 increased refractive index in the antenna surroundings, and the appearance of an asymmetric
8 spectral line around 800 cm^{-1} . Such Fano-like interferences have already been the subject of
9 extensive studies in the literature [7, 12, 45-47]. In order to provide further support to the actual
10 interaction between the PDMS vibrational resonances and the plasmonic field of the antennas,
11 we also acquired reflection spectra after covering the antennas with a polymer (AZ-5214) having
12 similar refractive index to PDMS but very weak absorption features in the spectral window under
13 consideration (see also Section G of the Supporting Information). In this way, we obtained
14 correctly red-shifted reference antenna spectra that can be used for background subtraction from
15 those obtained from PDMS-covered antennas. Through this experiment, we are able to
16 demonstrate (see Fig. 3c) that the line-shape around 800 cm^{-1} is completely different for parallel
17 and perpendicular polarization and that the line-shape obtained for perpendicular polarization is
18 similar to the one obtained from nominally undoped antenna samples. This observation clearly
19 highlights the electromagnetic coupling between PDMS and the longitudinal plasmon
20 resonances.
21
22
23
24
25
26
27
28
29
30
31
32
33
34
35
36
37
38
39
40
41
42
43
44
45

46 We also calculated (see Section H of the Supporting Information) the ratio between the
47 experimental spectra acquired from PDMS-coated antennas with parallel and perpendicular
48 polarization, both for the doped and undoped samples. Noticeably, the 800 cm^{-1} vibrational
49 feature from PDMS completely disappears in the undoped antennas after such normalization,
50 meaning that no PDMS-antenna interaction is taking place irrespective of the field polarization.
51
52
53
54
55
56
57
58
59
60

1
2
3 On the other side, a clear Fano-like line survives when the same normalization is performed for
4
5 doped antenna samples, again unambiguously highlighting the role of longitudinal localized
6
7 plasmon resonances.
8
9

10
11 We now focus our attention on the gap antennas, which display the strongest field
12
13 enhancement. Fig. 4a (left panel) provides a comparison between the spectra acquired with the
14
15 polarization parallel (solid line) and perpendicular (dashed line) to the antenna axis. The
16
17 experimental results compare well with those from numerical simulations, also presented in Fig.
18
19 4a (right panel). It should be noted here that, as observed in the SEM image in Fig. 3a, the
20
21 PDMS does not conformally cover the antenna gap, rather a PDMS meniscus is created due to
22
23 the surface tension. This is fully taken into account in the simulations. Clearly, since the hotspots
24
25 related to the R2 resonance are located right at the upper antenna edges, where the PDMS
26
27 adheres almost perfectly to the antenna, this does not compromise the sensing experiment. The
28
29 use of an antenna resonance with the associated field hotspots located in the air half space is
30
31 therefore confirmed to be an interesting feature that simplifies the requirements for analyte
32
33 delivery into the antenna gap.
34
35
36
37
38
39

40
41 In order to further clarify the role of the plasmonic hotspots, we also ran two separate
42
43 simulations (see Fig. 4b), a first one with PDMS placed only in the hotspots (black lines in Fig.
44
45 4c) and a second one with the PDMS coating everywhere except in the hotspots (red lines in Fig.
46
47 4c). The total PDMS volume in the former simulation is about 100 times smaller than in the
48
49 latter. In the left panel of Fig. 4c, for the perpendicular field polarization and PDMS only in the
50
51 hotspots, the simulations do not display any detectable sign of the PDMS vibrational mode at
52
53 800 cm^{-1} . On the contrary, when the PDMS coating is everywhere except in the hotspots the
54
55 vibrational mode is clearly visible. This behavior is at complete variance with what observed in
56
57
58
59
60

1
2
3 the right panel of Fig. 4c, i.e. for electric field polarization parallel to the antenna axis. Therein,
4
5 one clearly observes that the PDMS absorption line is visible in both simulations (PDMS only in
6
7 the hot spots and PDMS everywhere else). Indeed, while having a different line-shape because of
8
9 the interaction with the plasmonic resonance when the PDMS is in the hotspots, the two
10
11 vibrational features have roughly the same spectral weight, indicating that the respective
12
13 perturbations to the antenna spectrum have similar strengths. Since the simulated PDMS volume
14
15 in the hotspots only is about 100 times smaller than outside the hotspots, we estimate an
16
17 enhancement factor of up to two orders of magnitude for the optical signal generated by the
18
19 PDMS in the hotspots, compared to the PDMS outside the hotspots.
20
21
22
23
24

25
26 It is important here to stress that the experimentally observed line shape (Fig. 4a, left panel) is
27
28 interpreted as the far-field interference of the two contributions outlined in Fig. 4c for the parallel
29
30 polarization (black and red lines in the right panel). Their individual line shapes are determined
31
32 by two mechanisms: on the one side, the reflection geometry is known to produce Fano-like
33
34 features because of the interference between the light interacting with the PDMS layer and that
35
36 directly reflected by the substrate [46]. On the other side, we have the interaction between the
37
38 PDMS and the antenna resonance in the hot spots. The situation is further complicated by the
39
40 presence of shoulders and side peaks in the PDMS vibrational feature around 800 cm^{-1} (see
41
42 Section F of the Supporting Information). The overall interference process between the two
43
44 contributions in Fig. 4c, each one carrying its own specific phase, is therefore not easy to
45
46 deconvolve, yet it is accurately described and predicted by full-wave simulations in Fig. 4a (right
47
48 panel). Incidentally, one may notice that the estimated two-order-of-magnitude enhancement in
49
50 the sensing experiment is slightly larger than the average local intensity enhancement expected
51
52 in the antenna hot spots (see Fig. 1). This must likely be ascribed to small uncertainties in the
53
54
55
56
57
58
59
60

1
2
3 dielectric description of the Ge/PDMS system and in the evaluation of the enhancement for the
4 sensing experiment. , an intriguing possibility is also that the sensing enhancement might be
5
6 proportional to the square of the local intensity enhancement, as already pointed out in Ref. 48,
7
8 since the antenna works both as a receiving and as an emitting transducer for the electromagnetic
9
10 radiation.
11
12
13
14

15
16 Finally, we applied Ge plasmonic antennas to the sensing of chloroethyl methyl sulfide
17
18 (CEMS), a transparent liquid with mass density similar to that of water that is a simulant of
19
20 common explosive materials and cannot easily be distinguished from harmless liquids, except by
21
22 spectroscopy. During the experiment (Fig. 5a), the decrease in thickness of the droplet due to
23
24 evaporation was monitored with the same spectroscopy setup used for the sensing demonstration
25
26 by continuously acquiring fast FTIR spectra every 5 seconds and by measuring the period of the
27
28 Fabry-Pérot interference fringes in the near-IR. When the droplet thickness was estimated to be
29
30 below 2 μm , longer FTIR spectra with higher signal-to-noise ratio were acquired. Due to the
31
32 large volatility of the investigated substances, we are not able to quantitatively assess the exact
33
34 fraction of liquid inside and outside the hotspots, so to provide a precise value of the signal
35
36 enhancement due to the antennas. Fig. 5b demonstrates the IR absorption fingerprint spectrum of
37
38 the pure substance (grey line), obtained in transmission geometry with a 20- μm -thick IR cuvette.
39
40 A strong vibrational doublet appears at 690-720 cm^{-1} , i.e. below the plasma frequency of our
41
42 material in the region of plasmonic behavior, while a second fingerprint of similar vibrational
43
44 absorption strength appears around 1430 cm^{-1} in the region of dielectric behavior of the Ge, i.e.
45
46 above the plasma frequency. In Fig. 5c we also demonstrate the spectrum of the doped Ge
47
48 antennas covered with a droplet of CEMS (red line) superimposed onto the spectrum of the clean
49
50 antenna sample (black dashed line). By taking the difference between these two spectra, the
51
52
53
54
55
56
57
58
59
60

1
2
3 vibrational molecular fingerprint of CEMS is clearly recovered (Fig. 5d). One can notice,
4
5 however, that the relative spectral weight of the doublet at 690-720 cm^{-1} compared to the feature
6
7 at 1430 cm^{-1} in Fig. 5d is stronger than in the bare liquid material of Fig. 5b, thus qualitatively
8
9 pointing towards a signal enhancement provided by the plasmonic antenna response below the
10
11 plasma frequency of our material (see also Supporting Information, Section J).
12
13
14
15

16 In conclusion, we have introduced a novel all-group-IV semiconductor material platform for
17
18 mid-IR plasmonics, based on heavily doped Ge epitaxially grown on standard Si wafers. We
19
20 demonstrated localized plasmon resonances in Ge antennas and exploited the fabricated devices
21
22 for sensing experiments based on the resonant detection of molecular vibrational fingerprints of
23
24 both condensed-phase and liquid-phase analytes. While the present work demonstrates doping
25
26 levels of about $2.3 \cdot 10^{19} \text{ cm}^{-3}$, reaching a plasma frequency around 1000 cm^{-1} , the whole relevant
27
28 fingerprint region extending roughly up to 1800 cm^{-1} can be in principle reached given the high
29
30 solubility of P dopants in Ge [49] and the recent efforts to demonstrate carrier densities of the
31
32 order of 10^{20} cm^{-3} in n-type Ge [50]. Enhancement factors of up to two orders of magnitude for
33
34 the material located in the antenna hotspots have been obtained in the present work. Although the
35
36 demonstrated enhancement is still below that obtained with state-of-the-art Au antennas [8,13]
37
38 and the accessible wavelength range is slightly narrower than what has been obtained with III-V
39
40 compound semiconductor antennas [17], the demonstrated Ge antennas are compatible with the
41
42 silicon CMOS technology, which can in turn be used to build intelligent sensor networks with a
43
44 very large number of sensing elements at a far lower cost. As in most direct CMOS applications,
45
46 the performance of the single sensor must be traded for the number of identical sensors with
47
48 integrated readout electronics that can be realized, when compared with optimized stand-alone
49
50 antennas. The developed technology holds great promise for the realization of CMOS-
51
52
53
54
55
56
57
58
59
60

compatible mid-IR devices for substance-specific molecular sensing. The field enhancement in the plasmonic hotspots may also find applications in other fields where the on-chip integration of plasmonics with electronics is expected to play a key role, e.g. in IR imaging, light detection, and energy harvesting.

FIGURES

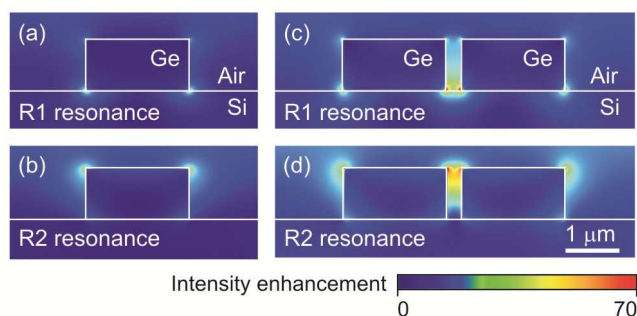
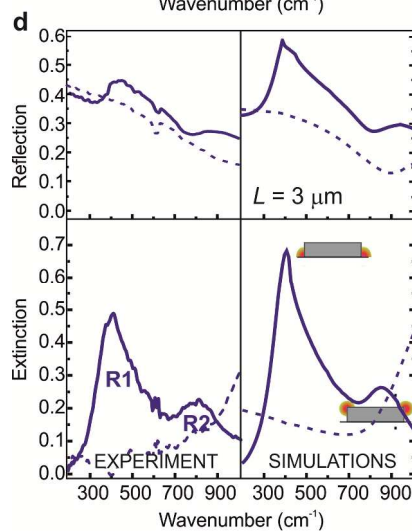
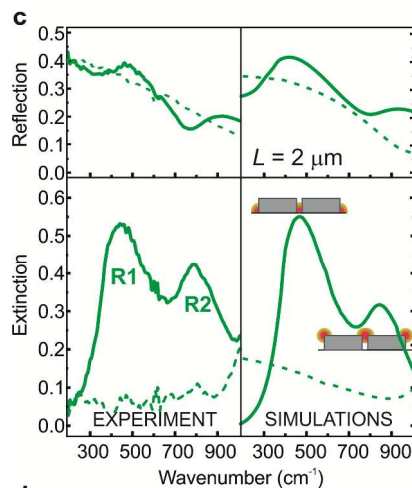
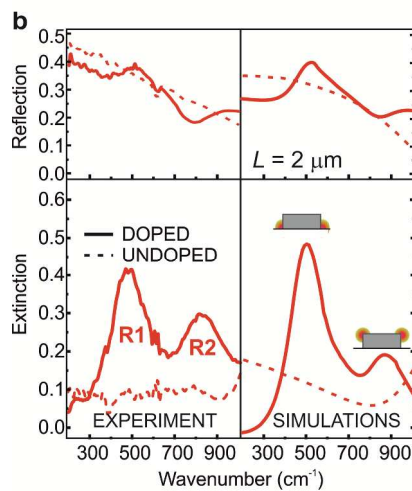
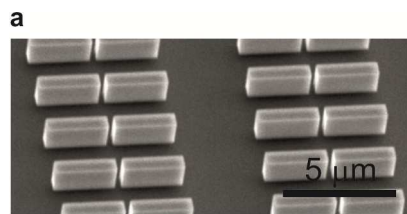


Figure 1. The field intensity distribution (squared modulus of the electric field) in the resonant Ge antennas: the simulated near-field intensity enhancement associated with the excitation of the localized plasmon modes labelled as R1 and R2 in the single-arm gapless antennas (a-b) and the double-arm gap antennas (c-d). All maps are calculated at the respective near-field resonance frequency. Each antenna arm is 2- μm long and the gap is 300 nm.



1
2
3
4
5
6
7
8
9
10
11
12
13
14
15
16
17
18
19
20
21
22
23
24
25
26
27
28
29
30
31
32
33
34
35
36
37
38
39
40
41
42
43
44
45
46
47
48
49
50
51
52
53
54
55
56
57
58
59
60

1
2
3 **Figure 2.** A demonstration of mid-IR plasmon resonances in Ge antennas: (a) a representative
4 SEM image of a Ge antenna sample. (b)-(d) The experimental and simulated reflection and
5 extinction spectra for single-arm antennas with $L = 2.0 \mu\text{m}$ length (b), gap antennas with $L = 2.0$
6 μm arm length (c), and single-arm antennas with $L = 3.0 \mu\text{m}$ length (d). The solid lines refer to
7 doped plasmonic antennas and the dashed lines refer to undoped non-plasmonic antennas. For
8 the sake of clarity, all the transmission spectra from the undoped antennas have been rescaled by
9 0.8 before the calculation of the normalized extinction ratio.
10
11
12
13
14
15
16
17
18
19
20
21
22
23
24
25
26
27
28
29
30
31
32
33
34
35
36
37
38
39
40
41
42
43
44
45
46
47
48
49
50
51
52
53
54
55
56
57
58
59
60

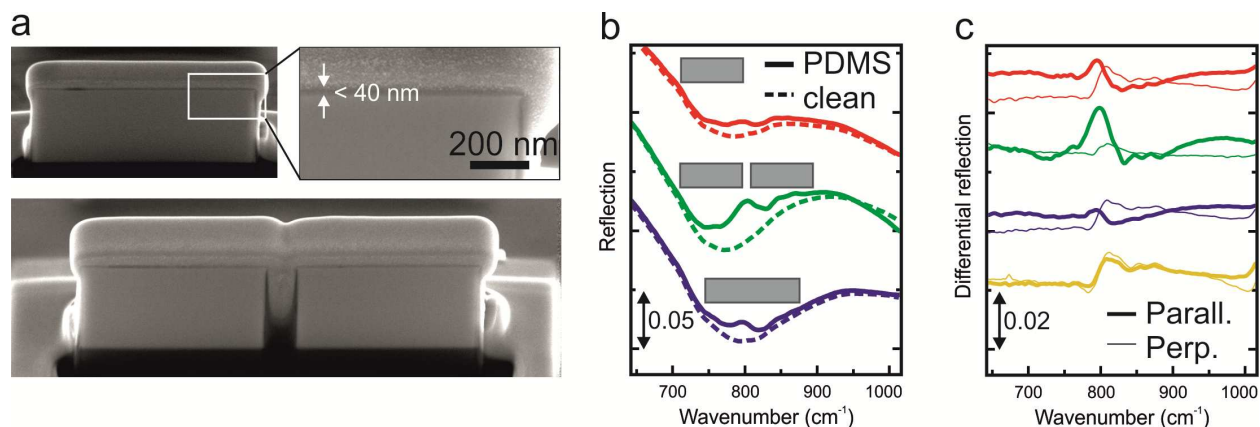


Figure 3. The solid-state sensing of a thin PDMS layer: (a) cross-sectional SEM images of the PDMS-covered antennas, obtained after deposition of a Pt overlayer with the slice-and-view technique in a dual-beam apparatus. The length of the single-arm antenna is $3\ \mu\text{m}$, while individual arms of the gap antenna are $2\ \mu\text{m}$ long. (b) The experimental reflection spectra acquired after PDMS spin coating on the three antenna samples (solid lines) and reference spectra from the clean samples (dashed lines); the spectra have been translated vertically for the sake of clarity. (c) The difference spectra obtained after subtraction of the spectra from antennas coated with AZ-5214; the spectra have been translated vertically for the sake of clarity. Thicker lines correspond to polarization parallel to the antenna axis, thinner lines to perpendicular polarization. The color coding is the same as in panel b and the yellow lines refer to an undoped antenna sample.

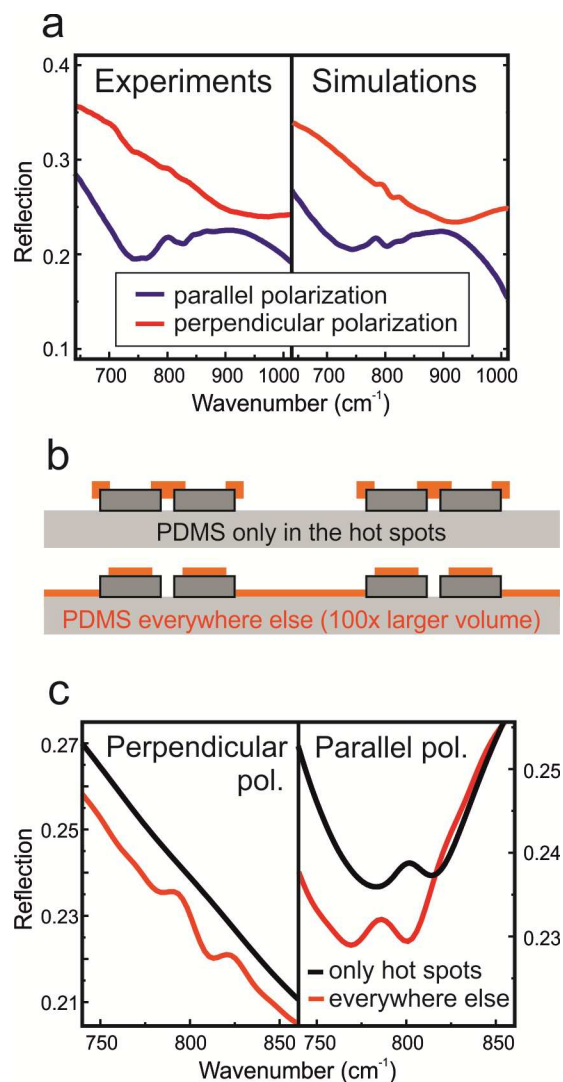


Figure 4. (a) The experimental (left panel) and simulated (right panel) reflection spectra from the PDMS-covered gap antenna sample, obtained with the field polarization parallel (blue line) or perpendicular (red line) to the antenna axis. The simulated spectra have been translated vertically for the sake of clarity. (b) Sketch of the PDMS distribution in the simulations demonstrated in panel c. (c) Simulations of reflection spectra highlighting the individual contributions coming from the antenna hot spots (black lines) and from everywhere else (red lines), for light with the polarization perpendicular to the antenna axis (left panel) and parallel to the antenna axis (right panel).

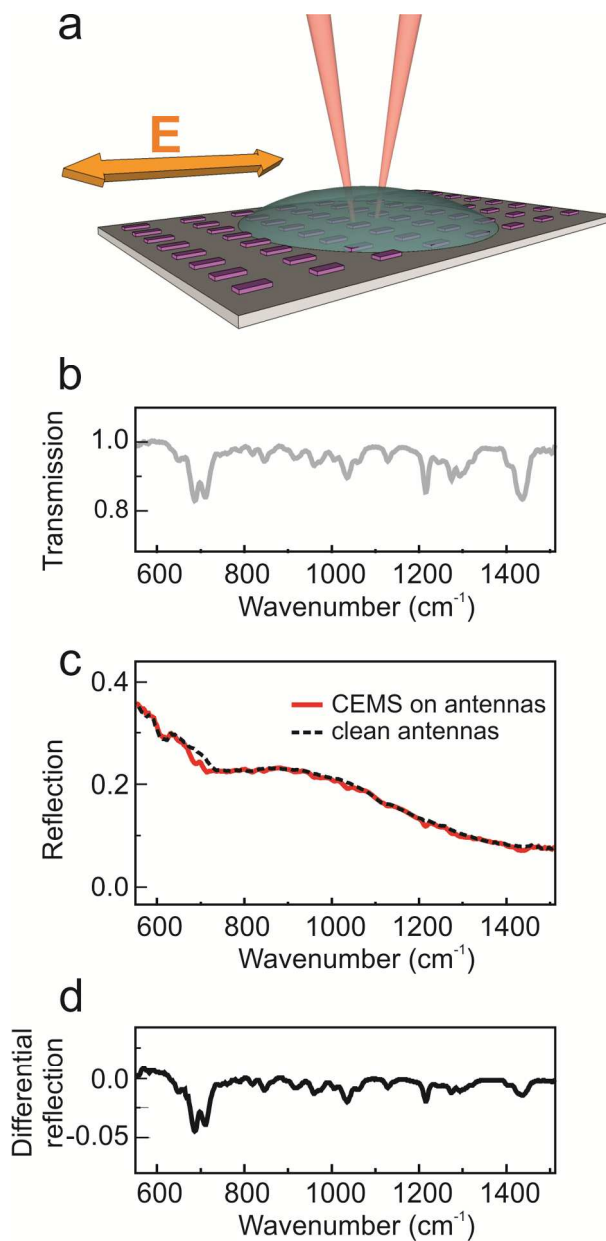


Figure 5. A hazardous liquid sensing experiment: (a) a sketch of the reflection sensing geometry; (b) the transmission spectrum of pure CEMS in a 20- μm -thick standard IR cuvette; (c) the reflection spectrum for a CEMS-covered antenna array (red line) and the reflection spectrum from the clean antenna array (black dashed line), and (d) the difference between the two spectra in panel c.

1
2
3 ASSOCIATED CONTENT
4
5

6
7 **Supporting Information.** Methods; dielectric constant extraction of the unpatterned Ge
8
9 material; electromagnetic simulations; geometrical details of the samples investigated in the
10
11 main manuscript; detailed analysis of the infrared spectra of the antenna arrays; absorbance
12
13 spectra of PDMS and CEMS; PDMS sensing: comparison with a weakly-absorbing polymer;
14
15 PDMS sensing: comparison with undoped antennas; PDMS sensing: role of the R1 resonance;
16
17 CEMS sensing: simulated near-field enhancement. This material is available free of charge via
18
19 the Internet at <http://pubs.acs.org>.
20
21
22
23
24
25

26 AUTHOR INFORMATION
27

28
29 **Corresponding Author**
30

31
32 *To whom correspondence should be addressed: paolo.biagioni@polimi.it
33
34

35 **Author Contributions**
36

37
38 ‡These authors contributed equally. J.F. and G.I. performed the growth of heavily-doped Ge on
39
40 Si. E.S. and P.B. performed the numerical simulations. A.S., K.G., and D.J.P. fabricated the
41
42 devices. L.B., E.C., and M.O. performed the FTIR characterization. P.B., M.O., and D.J.P.
43
44 coordinated the work and wrote the draft of the manuscript. All authors contributed extensively
45
46 to the analysis and discussion of the results and to the revision of the manuscript.
47
48
49

50
51 **Notes**
52

53
54 The authors declare no competing financial interest.
55
56
57
58
59
60

Funding Sources

The research leading to these results has received funding from the European Union's Seventh Framework Programme under grant agreement n°613055.

ACKNOWLEDGMENT

The authors would like to thank the staff of the James Watt Nanofabrication Centre for help in fabricating the samples and A. De Ninno and A. Notargiacomo of CNR-IFN-Rome for the PDMS film preparation and inspection by focused ion beam. Fruitful discussions with M. Bollani, D. Brida, M. Celebrano, S. Collin, L. Duò, M. Finazzi, and P. Ghenuche are gratefully acknowledged.

REFERENCES

- [1] Boltasseva A.; Atwater, H. A. *Science* **2011**, 331, 290-291.
- [2] Liu, N.; Tang, M. L.; Hentschel, M.; Giessen, H.; Alivisatos, A. P. *Nature Mater.* **2011**, 10, 631-636.
- [3] Svedendahl, M.; Chen, S.; Dmitriev, A.; Käll, M. *Nano Lett.* **2009**, 9, 4428-4433.
- [4] D'Andrea, C.; Bochterle, J.; Toma, A.; Huck, Ch.; Neubrech, F.; Messina, E.; Fazio, B.; Maragò, O. M.; Di Fabrizio, E.; de La Chapelle, M. L.; Gucciardi, P. G.; Pucci, A. *ACS Nano*, **2013**, 7, 3522-3531.
- [5] De Angelis, F.; Das, G.; Candeloro, P.; Patrini, M.; Galli, M.; Bek, A.; Lazzarino, M.; Maksymov, I.; Liberale, C.; Andreani, L. C.; Di Fabrizio, E. *Nature Nanotech.* **2010**, 5, 67-72.

- 1
2
3 [6] Adato, R.; Altug, H. *Nature Comm.* **2013**, 4, 2154-2163.
4
5
6 [7] Adato, R.; Artar, A.; Erramilli, S.; Altug, H. *Nano Lett.* **2013**, 13, 2584-2591.
7
8
9 [8] Adato, R.; Yanik, A. A.; Amsden, J. J.; Kaplan, D. L.; Omenetto, F. G.; Hong, M. K.;
10 Erramilli, S.; Altug, H. *Proc. Natl. Acad. Sci.* **2009**, 106, 19227-19232.
11
12
13 [9] Brown, L. V.; Zhao, K.; King, N.; Sobhani, H.; Nordlander, P.; Halas, N. J. *J. Am. Chem.*
14 *Soc.* **2013**, 135, 3688-3695.
15
16
17 [10] Limaj, O.; Lupi, S.; Mattioli, F.; Leoni, R.; Ortolani, M. *Appl. Phys. Lett.* **2011**, 98, 091902.
18
19
20 [11] Neubrech F.; Pucci, A.; Cornelius, Th. W.; Karim, S.; García-Etxarri, A.; Aizpurua, J. *Phys.*
21 *Rev. Lett.* **2008**, 101, 157403.
22
23
24 [12] Wu, C.; Khanikaev, A. B.; Adato, R.; Arju, N.; Yanik, A. A.; Altug, H.; Shvets, G. *Nature*
25 *Mater.* **2012**, 11, 69-75.
26
27
28 [13] Brown, L.V.; Yang, X.; Zhao, K.; Zheng, B.Y.; Nordlander, P.; Halas, N.J. *Nano Lett.* **2015**,
29 15, 1272-1280.
30
31
32 [14] Naik, G. V.; Shalaev, V. M.; Boltasseva, A. *Adv. Mater.* **2013**, 25, 3264-3294.
33
34
35 [15] Caldwell, J. D.; Lindsay, L.; Giannini, V.; Vurgaftman, I.; Reinecke, Th. L.; Maier, S. A.;
36 Glembocki, O. J. *Nanophotonics* **2015**, 4, 44-68.
37
38
39 [16] Law, S.; Podolskiy, V.; Wasserman, D. *Nanophotonics* **2013**, 2, 103-130.
40
41
42 [17] Law, S.; Yu, L.; Rosenberg, A.; Wasserman, D. *Nano Lett.* **2013**, 13, 4569-4574.
43
44
45
46
47
48
49
50
51
52
53
54
55
56
57
58
59
60

- 1
2
3 [18] Wang, T.; Nguyen, V. H.; Buchenauer, A.; Schnakenberg, U.; Taubner, Th. *Opt. Exp.* **2013**,
4
5 21, 9005-9010.
6
7
8
9 [19] N'Tsame Guilengui, V.; Cerutti, L.; Rodriguez, J.-B.; Tournié, E.; Taliercio, T. *Appl. Phys.*
10
11 *Lett.* **2012**, 101, 161113.
12
13
14 [20] Ginn, J. C.; Jarecky Jr., R. L.; Shaner, E. A.; Davids, P. S. *J. Appl. Phys.* **2011**, 110, 043110.
15
16
17
18 [21] Shahzad, M.; Medhi, G.; Peale, R. E.; Buchwald, W. R.; Cleary, J. W.; Soref, R.; Boreman,
19
20 G. D.; Edwards, O. *J. Appl. Phys.* **2011**, 110, 123105.
21
22
23 [22] Law, S.; Adams, D. C.; Taylor, A. M.; Wasserman, D. *Opt. Exp.* **20**, 12155-12165.
24
25
26
27 [23] Hoffman, A. J.; Alekseyev, L.; Howard, S. S.; Franz, K. J.; Wasserman, D.; Podolskiy, V.
28
29 A.; Narimanov, E. E.; Sivco, D. L.; Gmachl, C. *Nature Mater.* **2007**, 6, 946-950.
30
31
32 [24] Soref, R.; Hendrickson, J.; Cleary, J. W. *Opt. Exp.* **2012**, 20, 3814-3824.
33
34
35 [25] Biagioni, P.; Frigerio, J.; Samarelli, A.; Gallacher, K.; Baldassarre, L.; Sakat, E.; Calandrini,
36
37 E.; Millar, R. W.; Giliberti, V.; Isella, G.; Paul, D. J.; Ortolani, M. *J Nanophot.* **2015**, 9, 093789.
38
39
40 [26] Schwarz, B.; Reininger, P.; Ristanić, D.; Detz, H.; Andrews, A. M.; Schrenk, W.; Strasser,
41
42 G. *Nature Comm.* 2014, 5, 4085-4091.
43
44
45 [27] Palubiak, D.P.; Deen, M.J. *IEEE J. Select Topics Quant. Elec.* **2014**, 20, 6000718.
46
47
48
49 [28] Paul, D. J. *Elec. Lett.* **2009**, 45, 582-584.
50
51
52 [29] Soref, R. *Silicon* **2010**, 2, 1-6.
53
54
55 [30] Soref, R. *Nature Photon.* **2010**, 4, 495-497.
56
57
58
59
60

- 1
2
3 [31] Warburton, R. E.; Intermite, G.; Myronov, M.; Alfred, P.; Leadley, D. R.; Gallacher, K.;
4 Paul, D. J.; Pilgrim, N. K.; Lever, L. J. M.; Ikonc, Z.; Kelsall, R. W.; Huante-Ceron, E.; Knigts,
5 A. P.; Buller, G. S. *IEEE Trans. Elec. Dev.* **2013**, 60, 3807-3813.
6
7
8
9
10
11 [32] Rouifed, M. S.; Chaisakul, P.; Marris-Morini, D.; Frigerio, J.; Isella, G.; Chrastina, D.;
12 Edmond, S.; Le Roux, X.; Coudeville, J.-R.; Vivien, L. *Opt. Lett.* **2012**, 37, 3960-3962.
13
14
15
16
17 [33] Dumas, D. C. S.; Gallacher, K.; Rhead, S.; Myronov, M.; Leadley, D. R.; Paul, D. J. *Opt.*
18 *Exp.* **2014**, 22, 19284-19292.
19
20
21
22 [34] Jifeng L.; Sun. X.; Camacho-Aguilera, R.; Kimerling, L. C.; Michel, J. *Opt. Lett.* **2014**, 35,
23 679-681.
24
25
26
27
28 [35] Camacho-Aguilera, R. E.; Cai, Y.; Patel, N.; Bessette, J. T.; Romagnoli, M.; Kimerling, L.
29 C.; Michel, J. *Opt. Express* **2012**, 20, 11316-11320.
30
31
32
33 [36] Matmon, G.; Paul, D. J.; Lever, L.; Califano, M.; Ikonić, Z.; Kelsall, R. W.; Zhang, J.;
34 Chrastina, D.; Isella, G.; von Känel, H.; Müller, E.; Neels, A. *J. Appl. Phys.* **2010**, 107, 053109.
35
36
37
38 [37] Chaisakul, P.; Marris-Morini, D.; Frigerio, J.; Chrastina, D.; Rouifed, M.-S.; Cecchi, S.;
39 Crozat, P.; Isella, G.; Vivien, L. *Nat. Photon.* **2014**, 8, 482-488.
40
41
42
43
44 [38] Malik, A.; Dwivedi, S.; Van Landschoot, L.; Muneeb, M.; Shimura, Y.; Lepage, G.; Van
45 Campenhout, J.; Vanherle, W.; Van Opstal, T.; Loo, R.; Roelkens, K. *Opt. Expr.* **2014**, 22,
46 28479-28488.
47
48
49
50
51 [39] Chang, Y.-C.; Paeder, V.; Hvozdar, L.; Hartmann, J.-M.; Herzig, H. P. *Opt. Lett.* **2012**, 37,
52 2883-2885.
53
54
55
56
57
58
59
60

- 1
2
3 [40] TYDEX[®] materials and coatings database.
4
5
6 www.tydexoptics.com/materials1/for_transmission_optics/silicon (accessed August 13, 2015).
7
8
9 [41] Isella, G.; Chrastina, D.; Rössner, B.; Hackbarth, T.; Herzog, H.-J.; König, U.; von Känel,
10
11 H. *Solid State Electron.* **2004**, 48, 1317.
12
13
14 [42] Rosenblad, C.; Deller, H. R.; Dommann, A.; Meyer, T.; Schroeter, P.; von Känel, H. *J. Vac.*
15
16 *Sci. Technol. A* **1998**, 16, 2785-2780.
17
18
19
20 [43] Zuloaga, J.; Nordlander, P. *Nano Lett.* **2011**, 11, 1280-1283.
21
22
23
24 [44] Biagioni, P.; Huang, J.-S.; Hecht, B. *Rep. Prog. Phys.* **2012**, 75, 024402.
25
26
27 [45] Giannini, V.; Francescato, Y.; Amrania, H.; Phillips, Ch. C.; Maier, S. A. *Nano Lett.* **2011**,
28
29 11, 2835-2840.
30
31
32 [46] Svedendahl, M.; Käll, M. *ACS Nano* **2012**, 6, 7533-7539.
33
34
35 [47] Luk'yanchuk B.; Zheludev, N. I.; Maier, S. A.; Halas, N. J.; Nordlander, P.; Giessen, H.;
36
37 Chong, C. T. *Nature Mater.* **2010**, 9, 707-715.
38
39
40
41 [48] Alonso-González, P.; Albella, P.; Schnell, M.; Chen, J.; Huth, F.; García Etxarri, A.;
42
43 Casanova, F.; Golmar, F.; Arzubiaga, L.; Hueso, L. E.; Aizpurua, J.; Hillenbrand, R. *Nature*
44
45 *Comm.* **2012**, 3, 684-690.
46
47
48
49 [49] Vanhellefont, J.; Simoen, E. *Mater. Sci. Semicond. Proc.* **2012**, 15, 642-655.
50
51
52 [50] Klesse, W. M.; Scappucci, G.; Cappellini, G.; Hartmann, J. M.; Simmons, M. Y. *Appl. Phys.*
53
54 *Lett.* **2013**, 102, 151103.
55
56
57
58
59
60

1
2
3
4
5
6
7
8
9
10
11
12
13
14
15
16
17
18
19
20
21
22
23
24
25
26
27
28
29
30
31
32
33
34
35
36
37
38
39
40
41
42
43
44
45
46
47
48
49
50
51
52
53
54
55
56
57
58
59
60

Table of Contents Graphic

